Applied Physics Letters

A functional CMOS compatible MEMS pyroelectric detector using 12%-doped scandium aluminum nitride

Cite as: Appl. Phys. Lett. **117**, 183506 (2020); https://doi.org/10.1063/5.0024192
Submitted: 05 August 2020 • Accepted: 29 October 2020 • Published Online: 05 November 2020

D. K. T. Ng, T. Zhang, L. Y. Siow, et al.

Applied Physics Letters ARTICLE scitation.org/journal/apl

A functional CMOS compatible MEMS pyroelectric detector using 12%-doped scandium aluminum nitride

Cite as: Appl. Phys. Lett. **117**, 183506 (2020); doi: 10.1063/5.0024192
Submitted: 5 August 2020 · Accepted: 29 October 2020 ·
Published Online: 5 November 2020

D. K. T. Ng,[a] T. Zhang, L. Y. Siow, L. Xu, C. P. Ho, H. Cai, L. Y. T. Lee, Q. Zhang, and N. Singh

AFFILIATIONS

Institute of Microelectronics, A*STAR (Agency for Science, Technology and Research), 2 Fusionopolis Way, #08-02, Innovis Tower, Singapore 138634, Singapore

[a]Author to whom correspondence should be addressed: Doris_NG@ime.a-star.edu.sg

ABSTRACT

In this paper, we fabricate and demonstrate a functional complementary metal-oxide-semiconductor (CMOS) compatible pyroelectric uncooled thermal detector using 12% doped Scandium Aluminum Nitride (ScAlN) as the sensing layer. The ScAlN pyroelectric material is deposited at a temperature of ∼200 °C over an 8-in. wafer area. This detector has shown, in general, improved performance compared to AlN, with specific detectivity as high as $\sim 6.08 \times 10^7$ cm $\sqrt{\text{Hz}}/\text{W}$ and noise equivalent power as low as $\sim 8.85 \times 10^{-10}$ $\text{W}/\sqrt{\text{Hz}}$. The results show the specific detectivity of ScAlN-based pyroelectric detectors in the range of 10^7 cm $\sqrt{\text{Hz}}/\text{W}$, which is an improvement compared to AlN-based pyroelectric detectors which report specific detectivity typically in the range of 10^5–10^6 cm $\sqrt{\text{Hz}}/\text{W}$. This promising result opens up the opportunities for a CMOS compatible, 8-in. wafer-level manufacturable lead-free pyroelectric detector toward low cost and high throughput, allowing microelectromechanical systems (MEMS) and CMOS integration for increased applications in CMOS–MEMS integrated devices utilizing pyroelectric detectors.

There has been immense interest in uncooled thermal detectors as they promise a wide spectral wavelength of detection, all the way into the far infrared (IR) regime, which is desired for a wide range of applications such as gas sensing, thermal sensing, and thermal imaging.[1–3] In particular, the wavelength from 8 μm to 14 μm is especially useful for human body temperature detection.[4]

An attractive candidate is the pyroelectric thermal detector—one of its advantages is the ability to operate at room temperature, hence reducing the need for a liquid nitrogen (N_2) or helium (He) tank during operation as compared to photon detectors that require cryogenic cooling. This makes it possible for miniaturization of on-chip IR detectors based on pyroelectric thermal detectors as the device footprint is reduced due to the elimination of a bulky and expensive Dewar, which also requires regular maintenance.

Recently, there have been many reports[1,2,5,6] on aluminum nitride (AlN) as a pyroelectric material for applications toward room temperature thermal and IR detection. This is because as a pyroelectric material, AlN has favorable characteristics such as complementary metal-oxide-semiconductor (CMOS) compatibility, a high Curie temperature of around 2000 °C,[7,8] and not containing lead (Pb) and lithium (Li) contents as of conventional pyroelectric detectors. Currently, the main concern with using AlN as a pyroelectric detector is the relatively low pyroelectric coefficient of AlN, which is a main determining factor of its performance. Fuflyigin *et al.*[9] reported a pyroelectric coefficient of 6–8 μC/(m^2 K) for AlN, which is lower compared to that for lead zirconate titanate (PZT)[10,11] and lithium tantalate ($LiTaO_3$).[12]

To overcome this limitation, there have been attempts to dope AlN with Scandium (Sc) to increase the material pyroelectric coefficient. The interest to use Scandium Aluminum Nitride (ScAlN) for future microelectromechanical systems (MEMS) applications is fueled after a 40% increase in the piezoelectric coefficient is reported on 43% doped ScAlN.[13] In the area of ScAlN for pyroelectricity, so far there have been three papers[14–16] reporting on material studies of ScAlN, examining its pyroelectricity characteristics at the material level.

In this paper, we realize a MEMS pyroelectric thermal detector based on CMOS compatible 12% doped ScAlN. The ScAlN film is deposited at a temperature of ∼200 °C. The results of a 12% doped

ScAlN-based pyroelectric detector, in general, show specific detectivity improvement in the range of 10^7 cm $\sqrt{\text{Hz}}/\text{W}$, higher than that of the AlN pyroelectric detector typically reported[17–19] in the range of 10^5–10^6 cm $\sqrt{\text{Hz}}/\text{W}$. This opens up a whole new possibility of pushing up the performance of CMOS compatible MEMS pyroelectric detectors manufacturable on 8-in. wafers, allowing increased mass-production and low cost. Moreover, reports[15,16] on the higher pyroelectric coefficient by increasing the Sc doping concentration up to 35% give us the confidence that CMOS compatible MEMS pyroelectric detectors will eventually match performance with that of current commercially available $LiTaO_3$- and PZT-based pyroelectric detectors.[20,21]

Figure 1(a) shows a brief schematic of the fabrication flow of our ScAlN-based pyroelectric detector. Fabrication of these detectors is done using 8-in. wafers. First, an 8-in. wafer is patterned and etched to form trenches of around 1 μm wide and 5 μm deep. Next, these trenches are filled with tetraethyl orthosilicate (TEOS) low pressure chemical vapor deposition (LPCVD) silicon dioxide (SiO_2) and up to a layer thickness of around 1 μm to form an array of SiO_2 ribs. This layer structure of the SiO_2 rib array helps to increase mechanical stiffness to the device. The SiO_2 material acts as a thermal isolation material, to help to form thermal isolation on the final device structure. After SiO_2 layer deposition, chemical mechanical polishing (CMP) is then done on the SiO_2 layer to make the surface flat. Subsequently, a molybdenum (Mo) bottom electrode of around 200 nm thickness is deposited by sputtering and patterned by photolithography and inductively coupled plasma (ICP) etching. 12% doped ScAlN sensing material targeting at a thickness of 1 μm is subsequently deposited by sputtering. We use a 12% doped ScAlN sputtering target of around

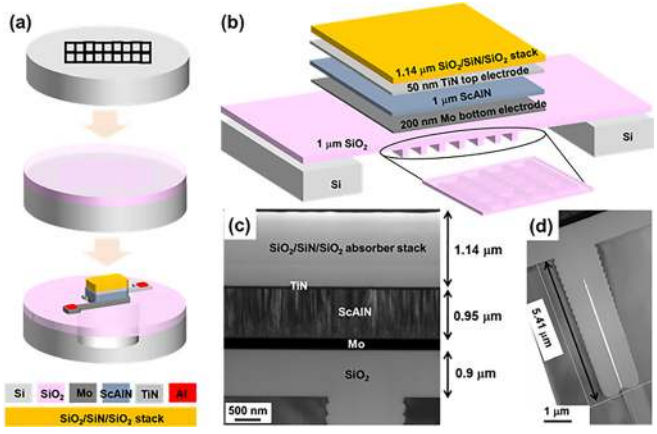

FIG. 1. (a) Brief schematic on fabrication flow of the pyroelectric detector. Trenches are first etched and filled with SiO_2 to form a layer for mechanical stiffness. CMP is then done on the SiO_2 layer to make the surface flat. Subsequent layers of Mo, ScAlN, TiN, absorber stack, and Al are deposited and patterned to form the detector structure. Finally, DRIE is done to release the backside Si for increased thermal isolation. (b) Schematic of the pyroelectric detector showing each layer structure and their respective thicknesses. A magnified schematic image of the SiO_2 rib array is also shown. The ribs are designed to have a width of 1 μm, a length of 5 μm, and a pitch of 10 μm. (c) Cross-sectional TEM image of the fabricated pyroelectric detector. Fabricated thicknesses are measured and shown. (d) Cross-sectional TEM image on the zoom-in of the deep trench filled with SiO_2 for added mechanical stiffness. The depth of the trench measures around 5.41 μm.

diameter 12-in. to deposit the ScAlN film at a processing temperature of ~200 °C. Lithography and etching are subsequently done to pattern this ScAlN film on top of the bottom electrode. Titanium Nitride (TiN) is then sputtered and patterned on top of ScAlN to form the top electrode. The last few steps include blanket deposition of an absorber stack consisting of the SiO_2-silicon nitride (SiN)-SiO_2 structure covering the electrodes. Patterning is then done to expose the Mo and TiN electrodes, and aluminum (Al) is deposited and goes through the wet etch process to form Al metal contacts on the respective electrodes. The final step is a two-step Si etching process, which includes the deep reactive ion etching (DRIE) process for bulk Si etching followed by the xenon difluoride (XeF_2) release process to remove the remaining Si substrate, leaving behind the pyroelectric detector in a membrane form. This will help in further thermal isolation on the detector device, having air as the thermal conduction medium instead of Si. Figure 1(b) shows the layer stack and each layer thickness of the pyroelectric detector. A magnified schematic image of the SiO_2 rib array is also shown. These SiO_2 ribs are designed to have a width of 1 μm, a length 5 μm, and a pitch 10 μm. Cross-sectional transmission electron microscopy (TEM) is done on the fabricated structure. Figure 1(c) shows the cross-sectional TEM image of the pyroelectric detector fabricated. Each layer is defined and the layers are measured. The entire detector stack has a thickness of around 3 μm. ScAlN deposited measures a thickness of 0.95 μm, which is around the 1 μm thickness that we targeted. The actual thickness shows a thickness drop of 50 nm due to the film uniformity variation of ±5%. The targeted thickness of 1 μm is chosen as too thin a ScAlN layer will result in higher capacitance and hence longer response time. A thicker ScAlN layer will help in shortening the detector's response time, but too thick a film might pose increased process challenges such as requiring a thicker etch mask, increased difficulties in controlling film uniformity, and stress. Hence, we choose a ScAlN thickness of 1 μm as a starting baseline in this work. This thickness of 1 μm is also consistent with the ScAlN film thickness reported[15,16] for ScAlN pyroelectric studies. Kurz *et al.*[15] used a thickness of 900 nm and Bette *et al.*[16] used a thickness of 1 μm for their ScAlN films. Figure 1(c) also shows that the ScAlN layer exhibits columnar-like structures in the film layer, revealing c-axis orientation. Figure 1(d) focuses on the trench at the bottom of the structure deposited with SiO_2. The trench is measured to be around 5.41 μm deep, almost filled with SiO_2 with slight void at the center of the trench to form the SiO_2 rib array. As etching is done by the Bosch process, scalloping is observed on the sidewall of the trench.

Figure 2(a) shows a photo image of the fabricated ScAlN-based pyroelectric detector die wire-bonded on a Transistor Outline (TO)-39 header. The die occupies an effective area of 3 mm × 1.8 mm. The respective Al metal contact pad of the top and bottom electrodes is each wire-bonded to one of the leads of the TO-39 header. Figure 2(b) shows a microscopy image of the fabricated ScAlN-based pyroelectric detector, which gives a magnified view of the detector die, sensing region, metal contact pads, and wire-bonded regions. The sensing area dimension is 536 μm × 536 μm. Each Al metal contact pad is sized at an area of 500 μm × 260 μm.

Each lead on the TO-39 is extended behind the header to be ~1.3 cm to allow easier connection for the measurement. The performance of the fabricated ScAlN-based pyroelectric detector is characterized using a commercial thermal MEMS based IR emitter (Axetris EMIRS50 AT06V) as the radiation source. This emitter is

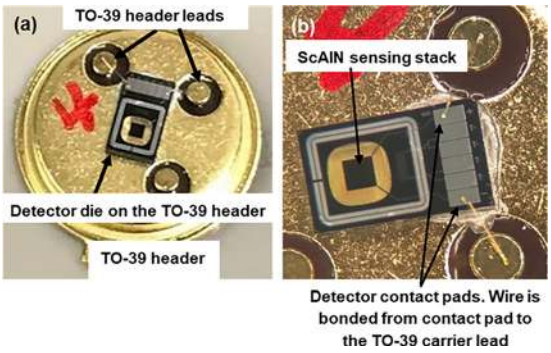

FIG. 2. (a) Photo image of the fabricated ScAlN-based pyroelectric detector die on a TO-39 header and wire bonded to the leads. The die dimension is 3 mm × 1.8 mm. (b) Microscopy image of this detector device showing the wires bonded to the TO-39 leads and the membrane sensing area at the center of the die. The area of the sensing area is 0.29 mm^2.

wire-bonded to another TO header and attached with a compound parabolic concentrator (CPC) to collimate the light from the emitter to the detector. The distance between the emitter and detector through the CPC is around 10 mm, which corresponds to an incident power of ∼10 μW at room temperature. The ScAlN-based pyroelectric detector device wire-bonded on TO-39 header is close-coupled to a commercial variable gain low noise current amplifier (DLPCA-200). The current amplifier is set at a gain of 10^9. The radiation power of the emitter source is modulated by a frequency of 1 Hz with a duty cycle of 50% to give a square wave Input to the detector. The signal output is recorded using an oscilloscope (Keysight infiniivision DSOX2012A).

Figure 3(a) shows the transient response output spectrum of the detector when the source emitter is set to modulate at a frequency of 1 Hz in the form of a square wave. The maximum current amplitude is measured to be around 1.99 nA. The polarity of output current corresponds to the "on" and "off" transition of the emitter's radiation modulating at 1 Hz. Upon receiving the square wave radiation from the source emitter, the pyroelectric detector senses an increase in temperature and exhibits a positive current peak. When the source emitter shuts off at the end of the square pulse, the pyroelectric detector senses a drop in temperature and exhibits a negative current peak as seen from the peaks in Fig. 3(a). This output spectrum is consistent with what was reported in the literature.[22,23]

Figure 3(b) shows a zoom-in spectrum of the pyroelectric detector at the rising edge of the square wave of the emitter. The total decay time is measured to be ∼145 ms. The thermal time constant is calculated by measuring the time taken for the current to drop by 63.2% from its peak value of ∼1.99 nA. The thermal time constant calculated is ∼33 ms. To get a measure of the pyroelectric coefficient of 12% doped ScAlN, the rise time of the pyroelectric detector is measured using the spectrum in Fig. 3(b). The rise time is measured to be ∼9.8 ms. This is the time taken for the current of the detector to rise to peak amplitude when triggered by the square wave irradiation of the emitter.

Concurrently, the temperature of the emitter source at a distance of 10 mm where the detector is located is measured using a platinum resistance temperature detector to record the temperature increase caused by the emitter's irradiation. The temperature increased measured is ∼8 K.

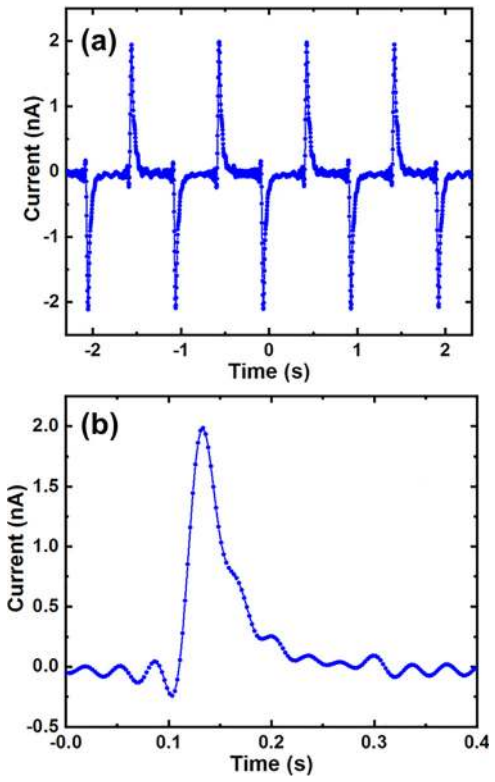

FIG. 3. (a) Output spectrum of current (nA) against time (s) measured from the ScAlN-based pyroelectric detector upon irradiation from the emitter source input with a square wave input. The current amplitude measured is around 2 nA. (b) Zoom-in spectrum of the pyroelectric detector's response at the rising edge of the square wave input. The thermal time constant is calculated to be ∼33 ms by analyzing the decay time.

The pyroelectric coefficient (ρ) of 12% doped ScAlN is then calculated using the following equation:[17,18,24]

$$\rho = \frac{i}{A(dT/dt)}, \tag{1}$$

where i is the current, A is the sensing area of the ScAlN-based pyroelectric detector, and dT/dt is the temperature change with time. Using (1), ρ calculated for 12% doped ScAlN is ∼8.35 $\mu C/m^2$ K. This is in agreement with what Kurz *et al.*[15] had reported.

The radiation power of the emitter is then set as a sinusoidal wave input to the pyroelectric detector. The output response from the detector is then measured by a lock-in amplifier (Zurich instruments HF2LI) when the emitter source is set to modulate at a certain frequency. In this case, we choose five different frequencies—7 Hz, 9 Hz, 11 Hz, 13 Hz, and 18 Hz. Based on the measured results, the current amplitudes after Fast Fourier Transform (FFT) at each respective frequency are recorded. Using these current amplitudes, the current-domain responsivity ($R_{I,xHz}$) at each respective frequency is calculated using the following equation:

$$R_{I,xHz} = \frac{I_{out,xHz}}{P_{in,xHz}}, \tag{2}$$

where $I_{out,xHz}$ is the current amplitude after FFT is measured at x Hz of the pyroelectric detector and $P_{in,xHz}$ is the equivalent radiation power from the emitter, where $P_{in,xHz} = \frac{P_{peak}}{\sqrt{2}}$. P_{Peak} is the incident power of the source emitter and the factor $\frac{1}{\sqrt{2}}$ is for normalization of the incident power. Figure 4 shows a plot of the device's current responsivity against frequency at each of the five frequencies chosen. From these five frequencies, we observe an increasing trend in the current responsivity as the frequency increases, with the lowest at 7 Hz, $R_{I,7Hz} \sim 1.44 \times 10^{-5}$ A/W and the highest at 18 Hz, $R_{I,18Hz} \sim 3.63 \times 10^{-5}$ A/W.

Focusing on the performance of the pyroelectric detector at 18 Hz, we further derive the noise equivalent power (*NEP*) and specific detectivity (D^*). Figure 5 shows plots of dark current and subsequent *NEP* and D^* calculated using various bandwidths (BWs) around 18 Hz radiation. The dark current is measured when the source emitter is totally switched off. Figure 5(a) shows the spectrum of the dark current after FFT analysis. Magnitude of the dark current is higher at lower frequency which we believe is caused by flicker noise. Beyond 10 Hz, the dark current is less than 5×10^{-14} A.

Using the data obtained from the dark current spectrum in Fig. 5(a) and the responsivity of ScAlN-based pyroelectric detector at 18 Hz, NEP is calculated using (3) at various noise *BWs* around 18 Hz,

$$NEP = \frac{I_N}{\sqrt{BW} \times R_{I,18Hz}}, \tag{3}$$

where I_N is the current noise calculated from the square root of the sum of square of current over the BW of interest and $R_{I,18Hz}$ is the responsivity of the detector at 18 Hz. Figure 5(b) shows the plot of *NEP* against various BW frequencies, up to 10 Hz maximum BW. The calculated *NEP* increases from $\sim 8.85 \times 10^{-10}$ W/$\sqrt{\text{Hz}}$ to $\sim 1.28 \times 10^{-9}$ W/$\sqrt{\text{Hz}}$ when the BW frequency increases from 1 Hz to 10 Hz.

With the calculated *NEP* and considering the area (A) of the pyroelectric detector ($A = 0.29\,\text{mm}^2$), the specific detectivity (D^*) is defined by

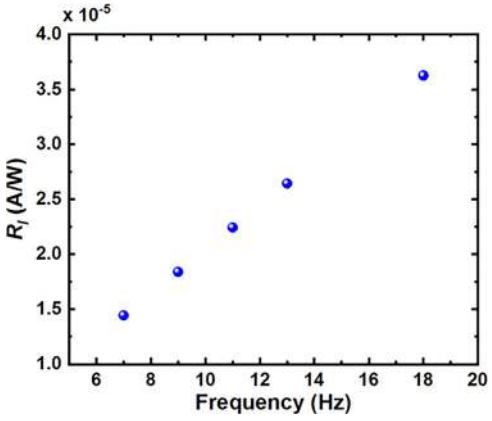

FIG. 4. Plot of current responsivity (R_I) against frequency for the ScAlN-based pyroelectric detector. Current responsivity is calculated from the response of the detector at five different frequencies. Minimum $R_{I,7Hz} \sim 1.44 \times 10^{-5}$ A/W at 7 Hz and maximum $R_{I,18Hz} \sim 3.63 \times 10^{-5}$ A/W at 18 Hz.

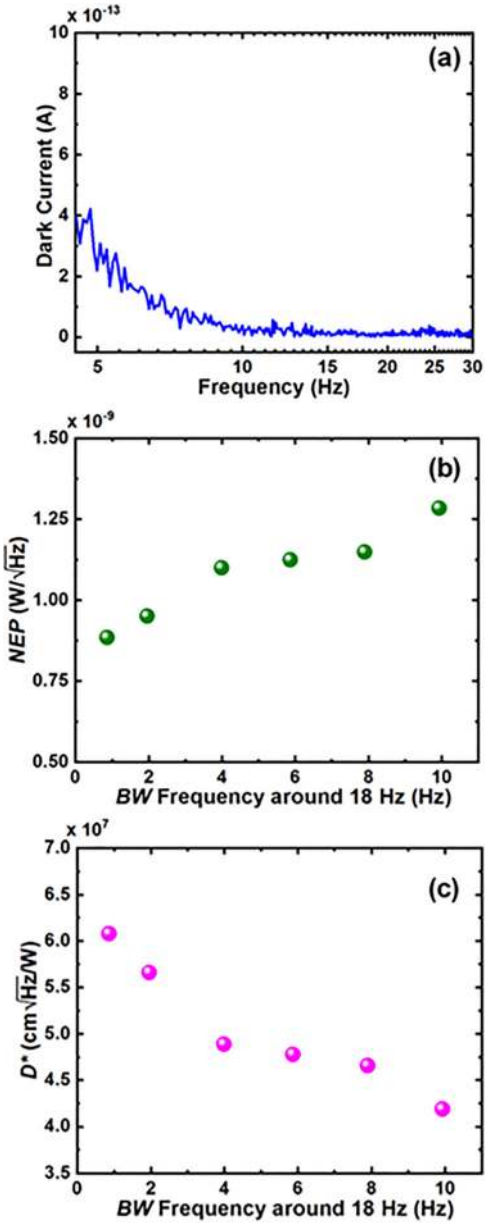

FIG. 5. (a) FFT spectrum of the dark current of the ScAlN-based pyroelectric detector in the frequency domain. (b) Plot of *NEP* against *BW* frequency from ~1 Hz to 10 Hz at around 18 Hz. The calculated *NEP* ranges from $\sim 8.8 \times 10^{-10}$ W/$\sqrt{\text{Hz}}$ to $\sim 1.28 \times 10^{-9}$ W/$\sqrt{\text{Hz}}$ across the *BW* frequency of 10 Hz. (c) Plot of D^* against *BW* frequency, showing D^* ranging from $\sim 4.19 \times 10^7$ cm $\sqrt{\text{Hz}}$/W to $\sim 6.08 \times 10^7$ cm $\sqrt{\text{Hz}}$/W across the *BW* frequency of 10 Hz. A detector performing at 18 Hz is chosen to calculate both *NEP* and D^*.

$$D^* = \frac{\sqrt{A}}{NEP}. \tag{4}$$

Figure 5(c) depicts the relationship between D^* and the BW frequency around 18 Hz. D^* calculated ranges from $\sim 6.08 \times 10^7$ cm $\sqrt{\text{Hz}}$/W at a BW frequency of ~1 Hz to $\sim 4.19 \times$

TABLE I. Summary on the performance of commercially available $LiTaO_3$ and PZT pyroelectric detectors and CMOS compatible AlN-based and ScAlN-based pyrodetectors. In general, ScAlN-based pyroelectric detectors have specific detectivity higher than what has been reported for AlN-based pyroelectric detectors, narrowing the performance gap between AlN and commercially available pyroelectric detectors.

Pyroelectric material platform		Size of sensing area, A (mm^2)	Noise equivalent power, NEP ($W/\sqrt{Hz}$)	Specific detectivity, D^* ($cm\sqrt{Hz}/W$)
Commercially available	PZT[21]	1	2.86×10^{-10}	3.5×10^{8}
	$LiTaO_3$[20]	4	1.11×10^{-9}	1.8×10^{8}
CMOS compatible	AlN[18]	0.25	5.3×10^{-9}	9.4×10^{6}
	AlN[19]	7	6.79×10^{-7}	3.9×10^{5}
	AlN[17]	0.29	8.87×10^{-9}	6.04×10^{6}
	12% Doped ScAlN (this work)	0.29	$\geq 8.85 \times 10^{-10}$	$\leq 6.08 \times 10^{7}$

10^7 cm $\sqrt{Hz}/W$ at a *BW* frequency of ~10 Hz. The performance of our ScAlN-based pyroelectric detector is in the range of 10^7 cm $\sqrt{Hz}/W$ in terms of D^*, which is about an order improvement compared to previous works[17–19] on an AlN-based pyroelectric detector, which typically reports D^* in the range of 10^5–10^6 cm $\sqrt{Hz}/W$.

Table I shows a summary of the performance of various pyroelectric detectors on different pyroelectric material platforms. Under the CMOS compatible platform, pyroelectric detectors realized by using AlN and 12% doped ScAlN (reported in this work) are presented in the table. As pyroelectric detectors presented by each group differ in designs, sizes, materials, and fabrication methods even when under the same material platform, we do not compare one directly with the other. The aim is to see the performance of ScAlN-based pyroelectric detectors. In general, 12% doped ScAlN-based pyroelectric detectors give a better specific detectivity performance, measured to be in the range of 10^7 cm $\sqrt{Hz}/W$, compared to AlN-based pyroelectric detectors, typically reported[17–19] to be in the range of 10^5–10^6 cm $\sqrt{Hz}/W$. This could be explained by the pyroelectric coefficient of ScAlN, which is the change in spontaneous polarization with temperature. Compared to AlN, ScAlN will experience a greater change in spontaneous polarization with temperature indicative by its increased pyroelectric coefficient as reported by Kutz *et al.*[15] and Bette *et al.*[16] With Sc doping in AlN, it has been shown experimentally[25] that there is an increase in the piezoelectric stress coefficient (e_{33}), which makes up part of the pyroelectric coefficient component.[15] An increase in e_{33} of ScAlN is due to the Sc substitution of Al, increasing the number of Sc–N bonds, which in turn soften the wurtzite crystal structure toward hexagonal boron-nitride structure, resulting in a decrease in the elastic constant and an increase in e_{33} of the lattice.[26]

In this work, our experimental results show that the 12% doped ScAlN-based pyroelectric detector outperforms the AlN-based pyroelectric detector. Although this is still around an order of magnitude lower in specific detectivity performance compared to commercially available $LiTaO_3$ and PZT pyroelectric detectors, it could be envisioned that with the increasing Sc-doping concentration, even higher performing pyroelectric detectors based on the ScAlN platform could be realized and CMOS compatible pyroelectric detectors with performance comparable to commercially available $LiTaO_3$ and PZT pyroelectric detectors could soon be possible.

In conclusion, we have demonstrated functional CMOS compatible pyroelectric detectors based on 12% doped ScAlN as the pyroelectric sensing material. A deposition temperature of ~200 °C is used to grow the ScAlN films. The performance of ScAlN-based pyroelectric detector has, in general, improved. D^* is in the range of 10^7 cm $\sqrt{Hz}/W$ compared to AlN-based pyroelectric detectors in which D^* is typically in the range of 10^5–10^6 cm $\sqrt{Hz}/W$. We report 12% doped ScAlN-based pyroelectric detectors with *NEP* as low as $\sim 8.85 \times 10^{-10}$ $W/\sqrt{Hz}$ and D^* up to $\sim 6.08 \times 10^7$ cm $\sqrt{Hz}/W$. This encouraging result brings about the indication that with the increasing Sc doping concentration (>12%), the performance of ScAlN-based pyroelectric detectors could eventually be comparable to that of commercially available $LiTaO_3$ and PZT pyroelectric detectors, opening up the possibility to commercialize 8-in. manufacturable, CMOS compatible, low cost pyroelectric detectors. In addition, these ScAlN-based pyroelectric detectors could further be integrated with emitter and waveguide components toward low cost, miniature, monolithic photonic gas sensors.

This work was supported by the Agency for Science, Technology and Research (No. IAF-PP A1789a0024). The authors thank E. J. Ng, Y. Gao, and Y. H. Fu for useful discussion and E. Wai and N. Jaafar for the wire-bonding support.

DATA AVAILABILITY

The data that support the findings of this study are available from the corresponding author upon reasonable request.

REFERENCES

[1]K. Yamamoto, F. Goericke, A. Guedes, G. Jaramillo, T. Hada, A. P. Pisano, and D. Horsley, Appl. Phys. Lett. **104**, 111111 (2014).
[2]E. Crisman, A. Drehman, R. Miller, A. Osinsky, D. Volovik, and V. Vasilyev, Phys. Status Solidi C **11**, 517 (2014).
[3]R. W. Whatmore, Rep. Prog. Phys. **49**, 1335 (1986).
[4]S. B. Lang, Phys. Today **58**(8), 31 (2005).
[5]N. Calvano, P. Chrostoski, A. Voshell, K. Braithwaite, and M. Rana, in *Wide Bandgap Power Devices and Applications II: Proceedings of SPIE Optical Engineering + Applications, San Diego, California, USA, 23 August 2017*, edited by M. Matin, S. Chowdhury, and A. K. Dutta (SPIE, 2017), Vol. 10381, pp. 103810J-1–103810J-8.
[6]B. Kebede, R. A. Coutu, and L. Starman, in *Micromachining and Microfabrication Process Technology XIX: Proceedings of SPIE MOEMS-MEMS, San Francisco, California, USA, 7 March 2014*, edited by M. A. Maher and P. J. Resnick (SPIE, 2014), Vol. 8973, pp. 89730I-1–89730I-10.
[7]R. Hou, D. Hutson, and K. J. Kirk, Insight-Non-destr. Test. Cond. Monit. **55**, 302 (2013).

[8]J. Sebastian, "Elevated temperature sensors for on-line critical equipment health monitoring," Technical Report No. UDR-TR-2004-00019 (2004).
[9]V. Fuflyigin, E. Salley, A. Osinsky, and P. Norris, Appl. Phys. Lett. **77**, 3075 (2000).
[10]R. Kohler, N. Neumann, N. Heβ, R. Bruchhaus, W. Wersing, and M. Simon, Ferroelectrics **201**, 83 (1997).
[11]R. Bruchhaus, D. Pitzer, M. Schreiter, and W. Wersing, J. Electroceram. **3**, 151 (1999).
[12]A. D'amico, G. Petrocco, A. Lucchesini, and F. Giannini, Mater. Lett. **3**, 33 (1984).
[13]M. Akiyama, K. Kano, and A. Teshigahara, Appl. Phys. Lett. **95**, 162107 (2009).
[14]V. Vasilyev, J. Cetnar, B. Claflin, G. Grzybowski, K. Leedy, N. Limberopoulos, D. Look, and S. Tetlak, MRS Adv. **1**, 2711 (2016).
[15]N. Kurz, Y. Lu, L. Kirste, M. Reusch, A. Zukauskaite, V. Lebedev, and O. Ambacher, Phys. Status Solidi A **215**, 1700831 (2018).
[16]S. Bette, S. Fichtner, S. Broker, L. Nielen, T. Schmitz-Kempen, B. Wagner, C. V. Buggenhout, S. Tiedke, and S. Tappertzhofen, Thin Solid Films **692**, 137623 (2019).
[17]D. K. T. Ng, G. Wu, T. Zhang, L. Xu, J. Sun, W. W. Chung, H. Cai, Q. Zhang, and N. Singh, J. Microelectromech. Syst. **29**, 1199 (2020).
[18]C. Ranacher, C. Consani, A. Tortschanoff, L. Rauter, D. Holzmann, C. Fleury, G. Stocker, A. Fant, H. Schaunig, P. Irsigler, T. Grille, and B. Jakoby, Sensors **19**, 2513 (2019).
[19]J. W. Stewart, J. H. Vella, W. Li, S. Fan, and M. H. Mikkelsen, Nat. Mater. **19**, 158 (2020).
[20]See https://www.infratec-infrared.com/downloads/en/sensor-division/detector_data_sheet/infratec-datasheet-lme-351-_.pdf for "InfraTec: Datasheet LME-351-# On Commercial Pyroelectric Detector" (last accessed August 2, 2020).
[21]See https://pyreos.com/wp-content/uploads/2019/07/Pyreos-Analog-TO-Sensor-One-Channel-Datasheet.pdf for "Pyreos Sensor Innovation Datasheet PY-ITV-SINGLE-TO39(2 + 1) (Rev.6.4) On Commercial Pyroelectric Detector" (last accessed September 7, 2020).
[22]S. P. Gaur, K. Rangra, and D. Kumar, Sens. Actuators, A **300**, 111660 (2019).
[23]I. Lubomirsky and O. Stafsudd, Rev. Sci. Instrum. **83**, 051101 (2012).
[24]A. Hossain and M. H. Rashid, IEEE Trans. Ind. Appl. **27**, 824 (1991).
[25]M. A. Caro, S. Zhang, T. Riekkinen, M. Ylilammi, M. A. Moram, O. Lopez-Acevedo, J. Molarius, and T. Laurila, J. Phys. **27**, 245901 (2015).
[26]K. R. Talley, S. L. Millican, J. Mangum, S. Siol, C. B. Musgrave, B. Gorman, A. M. Holder, A. Zakutayev, and G. L. Brennecka, Phys. Rev. Mater. **2**, 063802 (2018).